RSC Advances

PAPER

View Article Online
View Journal | View Issue

Cite this: *RSC Adv.*, 2015, **5**, 47174

A versatile bio-inspired material platform for catalytic applications: micron-sized "buckyball-shaped" TiO_2 structures

Deniz Altunoz Erdogan,[a] Touradj Solouki[b] and Emrah Ozensoy*[a]

Received 9th March 2015
Accepted 20th May 2015

DOI: 10.1039/c5ra04171f

www.rsc.org/advances

A simple sol–gel synthesis method is presented for the production of micron-sized buckyball-like TiO_2 architectures using naturally occurring *Lycopodium clavatum* (LC) spores as biotemplates. We demonstrate that by simply altering the calcination temperature and titanium(IV) isopropoxide : ethanol volume ratio, the crystal structure and surface composition of the buckyball-like TiO_2 overlayer can be readily fine-tuned. After the removal of the biological scaffold, the unique surface morphology and pore structure of the LC biotemplate can be successfully transferred to the inorganic TiO_2 overlayer. We also utilize photocatalytic degradation of Rhodamine B dye samples to demonstrate the photocatalytic functionality of these micron-sized buckyball-like TiO_2 architectures. Moreover, we show that the photocatalytic activity of TiO_2 overlayers can be modified in a controlled manner by varying the relative surface coverages of anatase and rutile domains. These results open a potential gateway for the synthesis of a variety of bio-inspired materials with unique surface properties and shapes comprised of reducible metal oxides, metal sulfides, mixed-metal oxides, and/or perovskites.

Introduction

Natural biological systems have served as efficient templates and inspired the design and production of novel synthetic materials with unprecedented surface morphologies, shapes, and compositions.[1–7] This versatile fabrication approach paves the way to the straightforward synthesis of unique and sophisticated surface structures which are difficult to attain even by utilizing the most advanced bottom-up synthetic methodologies. For example, biotemplate architectures with complex hierarchical pore structures may enable the synthesis of novel materials with exceptional pore sizes and pore geometries. Various biotemplates with dimensions ranging from 1 nm (*e.g.*, DNA)[3] to 1000 μm (*e.g.*, butterfly wings)[6] have been used to synthesize materials with different surface and structural properties. Such bio-inspired materials offer excellent opportunities to address modern technological needs in a variety of potential applications relevant to pharmaceuticals, biomedical systems, electronics, device manufacturing, energy storage/transformation/transfer, catalysis, molecular biology, and nanotechnology.[4,6–11]

Sol–gel chemistry can be utilized to develop simple, versatile, and inexpensive synthetic methods to grow inorganic (*e.g.*, metal oxide) thin film coatings on biological scaffolds.[1,3,6] By conserving the morphology/geometry of the underlying biological architectures, ordered overlayers with a wide range of thicknesses, ranging from a few nanometers to micrometers, can be manufactured.[1,3,6] For instance, to replicate the fine-structural details of a biotemplate, first, an inorganic precursor can be brought into contact with the self-assembled entities on the surface of the template. After the deposition/loading process, an organic–inorganic hybrid material can be obtained. Finally, this process can be followed by the removal of the biotemplate and transfer of the morphology/shape/geometry of the nascent biological scaffold to the inorganic overlayer structure. Calcination process is often employed to remove the organic template.[12] The use of such a thermal process for elimination of the biotemplate also offers an opportunity to fine-tune the structural properties of the inorganic film. It should be emphasized that during the thermal treatment process, undesirable deformation of the organic–inorganic hybrid material may also occur.[13–15] Thus, for an optimal biotemplating architecture, material properties of the organic (biological) and inorganic components should be structurally compatible. Furthermore, an ideal biotemplate should be inexpensive, mechanically and chemically adaptable, non-toxic, and abundant in nature. Based on the aforementioned requirements and considerations, botanical material platforms are excellent candidates for biotemplating. In particular, pollens and spores of various plants reveal moderately robust outer layers;[16] these biomaterials often display unique surface morphologies and pore structures, in the

[a]*Department of Chemistry, Bilkent University, 06800, Ankara, Turkey. E-mail: ozensoy@fen.bilkent.edu.tr; Fax: +90-312-266-4068; Tel: +90-312-290-2121*

[b]*Baylor University, Department of Chemistry & Biochemistry, Waco, TX, 76798, USA. E-mail: touradj_solouki@baylor.edu; Fax: +1-254-710-4272; Tel: +1-254-710-2678*

nanometer to micrometer range and can be readily utilized for biotemplating.

Titanium dioxide (TiO_2) has been widely used in the field of photocatalysis due to its high activity, chemical stability, environmentally friendly nature, and low-cost.[8,17,18] Here, we utilize *Lycopodium clavatum* (LC) spores[19,20] as efficient biotemplates, decorated with TiO_2 as an inorganic overlayer, and demonstrate the synthesis of a hierarchically-ordered novel material platform (*i.e.*, micron-sized buckyball-like TiO_2 architectures). LC is a commercially available, affordable, abundant, non-toxic, and versatile biomaterial (*e.g.*, it is commonly used in latent fingerprint development agents for forensic science applications).[21] In this study, we show that inorganic thin films such as TiO_2 can be coated on a LC biotemplate to mimic the pore structure and geometry of the underlying substrate. Furthermore, structural properties (*e.g.*, type and relative abundance of various polymorphs) of the TiO_2 overlayer can be fine-tuned *via* a simple calcination process, during the removal of the LC biotemplate. In addition, we demonstrate that by varying the synthesis parameters employed in the sol–gel process as well as the calcination protocol, functional properties of the bio-inspired final product can be controlled. By utilizing the TiO_2–LC hierarchical architectures in the photocatalytic degradation of Rhodamine B samples under UV illumination, we establish functional versatilities of these bio-inspired products. Current study opens a potential gateway for the synthesis of a large variety of future material platforms comprised of reducible metal oxide (*e.g.*, TiO_2, CeO_2, ZrO_2, ZnO, Fe_2O_3, Fe_3O_4 *etc.*), metal sulfide (*e.g.*, CdS, PbS *etc.*), mixed-metal oxide (*e.g.*, TiO_2–Al_2O_3, TiO_2–ZrO_2, CeO_2–ZrO_2, TiO_2–ZnO *etc.*), and/or perovskite (*e.g.*, $LaCoO_3$, $LaMnO_3$ *etc.*) systems with unprecedented surface/electronic/photonic/structural properties. These new materials could potentially play important roles in catalysis, energy, biology, medicine, and nanotechnology applications. The current study is also relevant to metal oxide growth mechanisms in biological templates and natural bio-mineralization processes.[22]

Experimental

Materials

Lycopodium clavatum (LC) spores, titanium(IV) isopropoxide (TIP, 97%), ethanol (≥99.8%), and Rhodamine B (RhB, dye content ~95%) were purchased from Sigma-Aldrich (Germany). All chemicals were used as received and without any further purification. Milli-Q deionized water (18.2 MΩ cm) was also used in the synthesis.

Material preparation

To obtain micron-sized buckyball-like TiO_2 architectures, a template-assisted synthetic strategy was employed. LC spores with an average diameter of ~27 μm were used as the initial biotemplate. A simple sol–gel process was applied by mixing the precursor (*i.e.*, TIP) with ethanol, using different TIP : ethanol volume ratios (3 : 2, 2 : 1, 3 : 1 v/v, respectively). While rigorously stirring this precursor solution at room temperature, 100 mg LC powder was slowly added to the mixture. After 30 min of mixing/immersion, LC spores were separated from the precursor solution by filtration. After filtration, TiO_x-coated LC microspheres were dried under ambient conditions. Dried samples were calcined in air at 200, 300, 400, 500, 600, 700, 800, and 900 °C in a muffle furnace for 3 h. Final batches of the products were named as *LcTi*(*X* : *Y*)-*T*, where "*X* : *Y*" represented the TIP : ethanol volume ratio and "*T*" indicated the calcination temperature.

Material characterization

The microscopic structure and the surface morphology of the synthesized samples were investigated with a scanning electron microscope (SEM, Carl-Zeiss Evo40) equipped with an energy dispersive X-ray (EDX) analyzer (Bruker AXS XFlash 4010). Samples for SEM and EDX analyses were prepared by mechanically dispersing the synthesized powders on an electrically conductive carbon film, which was placed on an aluminum sample holder. No additional coatings or dispersive liquids were used for the SEM and EDX samples. SEM images were obtained using a vacuum SE detector, where the acceleration voltage of the incident electron beam was varied within 5–10 kV range. All of the EDX data were collected using an electron acceleration voltage of 10 kV. To ensure the reproducibility of the EDX results for elemental analysis studies, at least four independent areas of identical dimensions were investigated on each sample.

The crystallographic structures of the samples were analyzed by using a X-ray diffractometer (Rigaku, Japan) equipped with a Miniflex goniometer where a monochromatic X-ray source (CuKα, $\lambda = 0.15405$ nm, 30 kV, 15 mA) was utilized. For the XRD measurements, samples were scanned within a 2θ range of 10–60° with a scan rate of 0.02° s^{-1}. Diffraction patterns were assigned using Joint Committee on Powder Diffraction Standards (JCPDS) cards supplied by the International Centre for Diffraction Database (ICDD).

Raman spectroscopic measurements were performed on a LabRAM HR800 spectrometer (Horiba Jobin Yvon, Japan) equipped with a Nd:YAG laser ($\lambda = 532.1$ nm) operated with a power of 20 mW and an integrated confocal Olympus BX41 microscope. Prior to conducting Raman measurements, the powder samples were mechanically dispersed onto a single-crystal Si substrate. The Raman spectrometer was regularly calibrated by adjusting the zero-order position of the grating and using the reference Si Raman shift at 520.7 cm^{-1}. Raman spectra were recorded in the range of 100–1500 cm^{-1} with a spectral resolution of 4 cm^{-1}.

Photocatalytic performance tests

Photocatalytic activities of the micron-sized buckyball-like TiO_2 architectures, under UVA irradiation, were evaluated using the discoloration rate of Rhodamine B (RhB) dye solutions.[23–26] A photocatalytic reactor (enabling continuous stirring of the dye-photocatalyst mixture) equipped with Sylvania UVA-lamps (F8W, T5, Black-light, 8 W, 368 nm) was employed in the photocatalytic activity tests. The total irradiation power measured at the sample position during the photocatalytic performance

tests was 9 W m^{-2}. The distance between the light source and the solution was kept fixed at 13 cm and the sample solution was isolated from other sources of irradiation during the photocatalytic degradation process. In a typical photocatalytic degradation experiment, a 45 mL aqueous suspension containing RhB (10 mg L^{-1}) and the photocatalyst (25 mg) was stirred for 1 h in dark in order to establish the adsorption–desorption equilibrium between the photocatalyst surface and RhB. Then, the suspension was irradiated with UVA photons and the variation in the RhB concentration was quantitatively monitored as a function of time. For this purpose, 3 mL aliquots were extracted from the dye-photocatalyst mixture after various irradiation time intervals. Then, the photocatalyst was separated from the aliquot *via* centrifugation. The collected liquid filtrate was analyzed using a Carry 300, Agilent UV-Vis spectrophotometer and by monitoring the characteristic RhB absorption wavelength (λ_{max}) around 553 nm. Under identical experimental conditions, photocatalyst-free RhB solution degradations were also carried out as control experiments. The photodegradation behavior of the photocatalyst was determined with respect to the relative concentration of RhB solution by plotting C/C_0 as a function of time, where C_0 and C represent concentrations of the test solution before and after irradiation, respectively. Then, the apparent first-order rate constant of the photocatalyst (k', min^{-1}) was calculated from the linear relationship between the ln C_0/C and irradiation time.

Results and discussion

Morphology and structure

Fig. 1, inset shows a typical SEM image of an uncoated LC spore. Experimentally observed average diameter of these LC spores is 27 ± 4 μm and their inner cores are composed of polysaccharides. However, external layers of these LC spores (*i.e.*, *exine capsule*) consist of a sturdy bio-polymer called *sporopollenin*.[16] The carbonaceous nature of LC spore's outer surfaces is also confirmed by EDX data. For example, the two major peaks in the EDX spectrum of an LC spore's outer surface (Fig. 1) predominantly correspond to C and O atoms. This robust outer layer protects the biological functionalities of LC systems against potentially harmful environmental stimuli (*e.g.*, mechanical stress, UV-light, temperature, chemicals, *etc.*). This outer surface is geometrically decorated with hierarchical pentagonal and hexagonal cavities/pockets which are separated by partitions (walls) with an average thickness of ~350 ± 70 nm (Fig. 1).

The biopolymer network on the surface of the LC biotemplate is capable of forming complexes with metal-alkoxide functionalities.[27,28] Thus, a simple sol–gel synthetic approach can be employed to deposit TIP on the outer shell of LC spores. By controlling the hydrolysis–condensation kinetics of TIP and the subsequent formation of the TiO_2 overlayer, it is feasible to coat the LC exine capsule without any major changes in the size/geometry, pore structure, and morphology of the biotemplate. Fig. 2 contains SEM and EDX data from analyses of a TIP-coated LC spore (*i.e.*, LcTi(2 : 1)-25) after aging at room temperature (*i.e.*, before calcination). As will be discussed in the next sections, this particular TIP loading revealed the highest photocatalytic activity. General characteristics and morphology of the samples with other TIP/EtOH ratios (data not shown) were rather similar. SEM images given in Fig. 2a and b show that a relatively uniform $TiO_x/Ti(OiPr)_4$ overlayer was deposited on the LC spore without the existence of neither extremely large (>100 nm) agglomerates of Ti-containing domains nor large patches of uncoated/bare LC biotemplate. This is also visible in the EDX line scan of the Ti signal across the TIP-coated LC spore (Fig. 2c) as well as the Ti and O elemental EDX mapping results given in Fig. 2e and f, respectively.

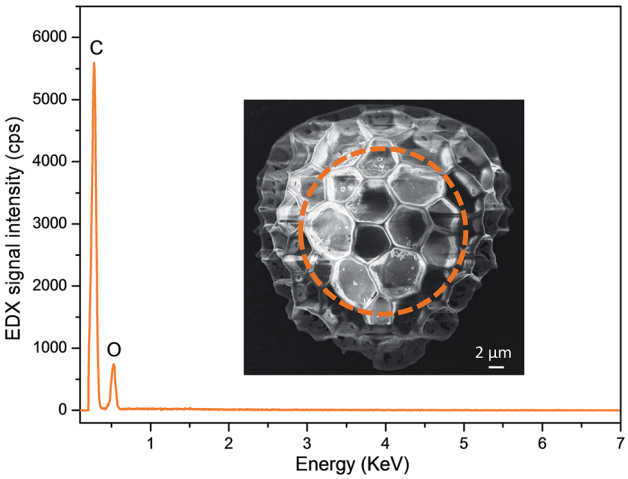

Fig. 1 SEM image and the corresponding EDX spectrum of an uncoated commercial *Lycopodium clavatum* (LC) biotemplate sample. Dashed region depicts the region where the EDX spectrum was acquired.

It is worth noting that the thickness of the $TiO_x/Ti(OiPr)_4$ overlayer can be conveniently modified by varying the amount of the Ti-precursor and/or immersion time of the biotemplate in the TIP/EtOH solution. For example, when the immersion time was decreased below 30 min, uncoated regions on the surface of the biotemplate were detected *via* EDX measurements (data not shown). On the other hand, for longer immersion times (*e.g.*, >60 min) local aggregations/clusters of $TiO_x/Ti(OiPr)_4$ overlayer were observed in SEM images (data not shown). Thus, an optimal immersion duration of 30 min was utilized in the synthesis protocol. To demonstrate the influence of the amount of Ti on the photocatalytic performance and chemical composition of the overlayer, precursor solutions with different TIP loadings (*i.e.*, LcTi(3 : 2), LcTi(2 : 1), and LcTi(3 : 1)) were used in the material synthesis. It was observed that by increasing TIP loading, LC surfaces became coarser at the nanometer scale and the thickness of the partitions or walls separating the polygon-shaped hierarchical cavities increased from ~350 nm to ~750 nm (*e.g.*, compare SEM images in Fig. 1 and 2b); while lower TIP loadings led to 2D islands/patches (that is existence of uncoated biotemplate domains). Thus, TIP loadings were varied between LcTi(3 : 1)–LcTi(3 : 2).

Calcination process was employed to transform the amorphous $TiO_x/Ti(OiPr)_4$ overlayer, obtained after room temperature TIP/EtOH deposition and successive aging, into various

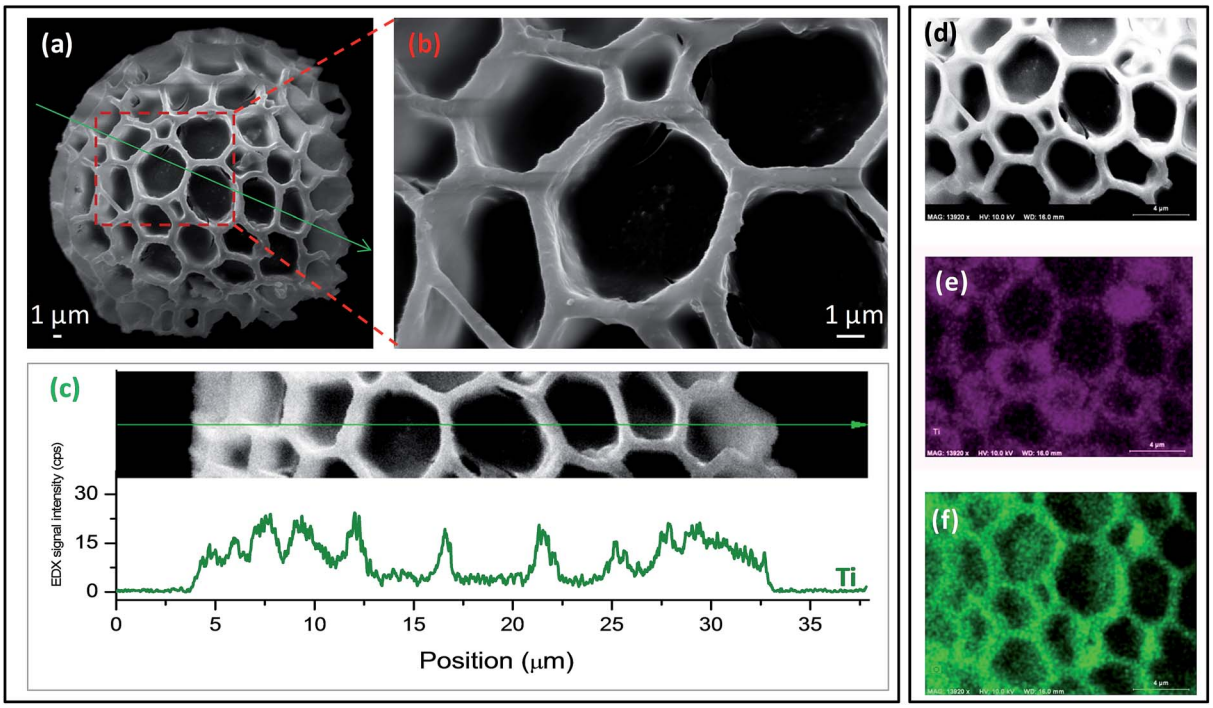

Fig. 2 LC biotemplate after titanium(IV) isopropoxide (TIP) deposition (*i.e.*, LcTi(2 : 1)-25 sample) at 25 °C: (a) low magnification SEM image; (b) higher magnification SEM image; (c) EDX line scan of the Ti signal across the TIP-coated LC spore along with the corresponding SE image; (d) SE image, and elemental EDX maps of (e) Ti (blue) and (f) O (green) signals.

ordered polymorphs of TiO_2 and remove the underlying LC biotemplate. To prevent major structural deformation of the biotemplate, before the formation of the micron-sized buckyball-like TiO_2 architectures, calcination parameters (*i.e.*, annealing ramp rate, calcination temperature, and external gaseous environment) were carefully optimized.

SEM images in Fig. 3 show that when LC spores are coated with a $TiO_x/Ti(OiPr)_4$ overlayer (*i.e.*, for LcTi(3 : 2) or LcTi(2 : 1)) and calcined at elevated temperatures (*e.g.*, 800–900 °C), micron-scale structural details of the pollen substrate are still preserved. Dimensions of the micron-sized buckyball-like TiO_2 architectures after calcination are also comparable to dimensions of the original LC spores. However, upon calcination, TiO_2 overlayer inside the cavities (or pockets) displayed sporadic cracks and holes (possibly due to the mechanical stress inflicted on the TiO_2 film during the high temperature treatment and removal of the LC substrate (Fig. 3a–c, f and g)). For example, the SEM image shown in Fig. 3f, corresponding to the LcTi(3 : 2)-800 sample, confirms that upon the high-temperature calcination, inner polysaccharide core of the LC structure as well as the exine capsule comprising of *sporopollenin* are eliminated to a large extent (though not entirely), revealing a hollow TiO_2 buckyball-shell. This is also spectroscopically confirmed by EDX analysis of the LcTi(2 : 1)-800 sample as shown in Fig. 3d and e. Fig. 3d and e show that C and O EDX signals originating from the core of the biotemplate drastically diminish upon calcination. Furthermore, Ti signal due to the TiO_2 buckyball-shell becomes significantly prominent. Fig. 3e also shows an EDX line scan of the elemental Ti signal illustrating that the Ti signal coincides with the corrugations on the LC spore which is consistent with the presence of a rather uniform TiO_2 coating on the LcTi(2 : 1)-800 sample surface. It is worth noting that the typical specific surface area of the LcTi(2 : 1)-800 sample obtained *via* Brunauer–Emmett–Teller (BET) method was $\sim$7.5 $m^2\ g^{-1}$.

The SEM and EDX data for LcTi(3 : 2)-400 sample (Fig. 4) demonstrate that low calcination temperatures such as 400 °C are insufficient to remove the polysaccharide core of the LC system. Fig. 4a shows two different regions: one located inside the inner core of the hollow capsule (marked with an empty red circle, corresponding to the underlying intact biotemplate substrate below the TiO_2 overlayer) and a second region corresponding to the outer surface of the hollow capsule (marked with an empty blue circle, on the periphery). EDX spectrum corresponding to the inner red zone (*i.e.*, inside the hollow capsule) is dominated by C and O signals without a significant contribution from the Ti signal; conversely, the EDX spectrum for the outer blue zone (*i.e.*, outermost surface) is dominated by Ti signals. These results are consistent with the thermogravimetric analysis (TGA) measurements in the literature,[29] which reported that while TiO_2 revealed a negligible gravimetric loss within 25–800 °C, uncoated *Lycopodium* spores underwent almost 60% weight loss within 250–450 °C due to thermal decomposition/degradation/oxidation processes.

Calcination process used for the removal of the LC biotemplate after the formation of the inorganic overlayer can be utilized as a tool to fine-tune the chemical composition and the crystallographic structure of the outermost layer. Such compositional properties were also characterized in detail *via* XRD as a function of the calcination temperature (as well as TIP/EtOH

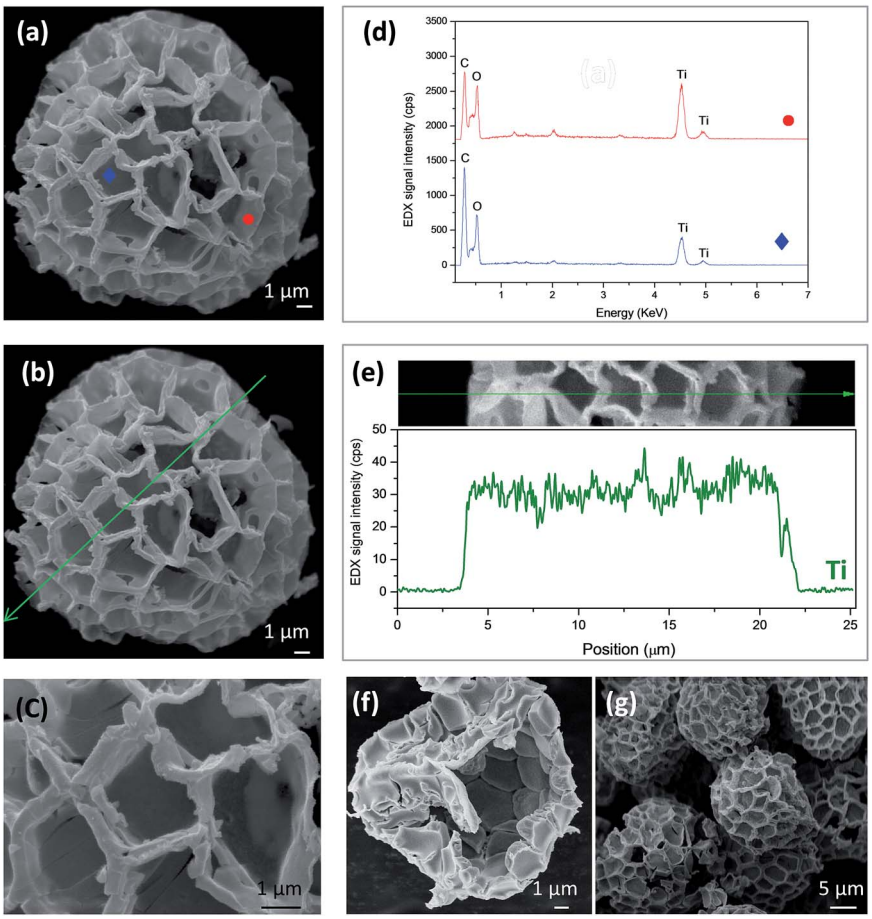

Fig. 3 (a–c) SEM images of the hollow micron-sized buckyball-like TiO_2 architectures calcined at 800 °C for 3 h in air (LcTi(2 : 1)-800); (d) EDX spot analysis for the corresponding points (*i.e.*, ● and ♦) given in (a); (e) line-scan analysis of EDX Ti-signal (green curve) along the line depicted in (b); SEM images of (f) LcTi(3 : 2)-800 and (g) LcTi(3 : 2)-900.

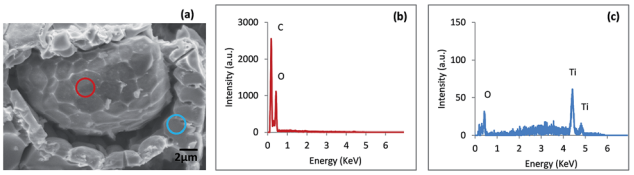

Fig. 4 SEM image (a) of the LcTi(3 : 2)-400 sample; corresponding EDX spectra representing (b) the interior seed part of the LC bio-template and (c) external TiO_2 buckyball-like shell.

ratio (Fig. 5)). XRD patterns revealed that anatase (ICDD card no.: 00-021-1272) signals (designated as "A" in Fig. 5) were the only prominent diffraction signals at $T \leq 500$ °C and became sharper with increasing temperatures suggesting ordering and increasing average particle size. At $T \geq 600$ °C, rutile (designated as "R" in Fig. 5) diffraction signals (ICDD card no.: 00-021-1276) started to appear and dominate the XRD patterns at elevated temperatures. When calcination temperatures below 400 °C were utilized, samples were found to contain mostly amorphous/disordered TiO_2/TiO_x phases.

The average crystallite sizes of the anatase and rutile phases were calculated based on the main XRD peaks corresponding to anatase (101) and rutile (110) signals using Scherrer equation as a function of precursor loading and calcination temperature (Fig. 6). As can be noted from the stacked column chart in Fig. 6, the crystallinity of TiO_2 domains typically increase with increasing calcination temperature. For all samples analyzed, anatase phase had a characteristically smaller average crystallite size than the rutile phase. Fig. 6 clearly demonstrates that the extent of crystallization depends both on the calcination temperature and precursor loading. It is also apparent that anatase to rutile phase transformation temperatures increase with increasing TIP loading in the initial precursor mixture. Relative mass fractions of anatase *versus* rutile phases were also calculated *via* Spurr and Myers approach (Table 1).[30] LcTi(2 : 1)-700 and LcTi(2 : 1)-800 samples (marked with bold numerals in Table 1, columns two and three), which exhibited two of the highest photocatalytic activity values, revealed a phase composition where anatase and rutile phases had similar mass percentiles (*i.e.*, ~50% anatase and ~50% rutile).

As a complementary characterization technique, Raman spectroscopy was also employed for the structural analysis of the micron-sized buckyball-like TiO_2 architectures as a function of calcination temperature and TIP loading. In general, Raman spectra presented in Fig. 7 were in very good agreement with the

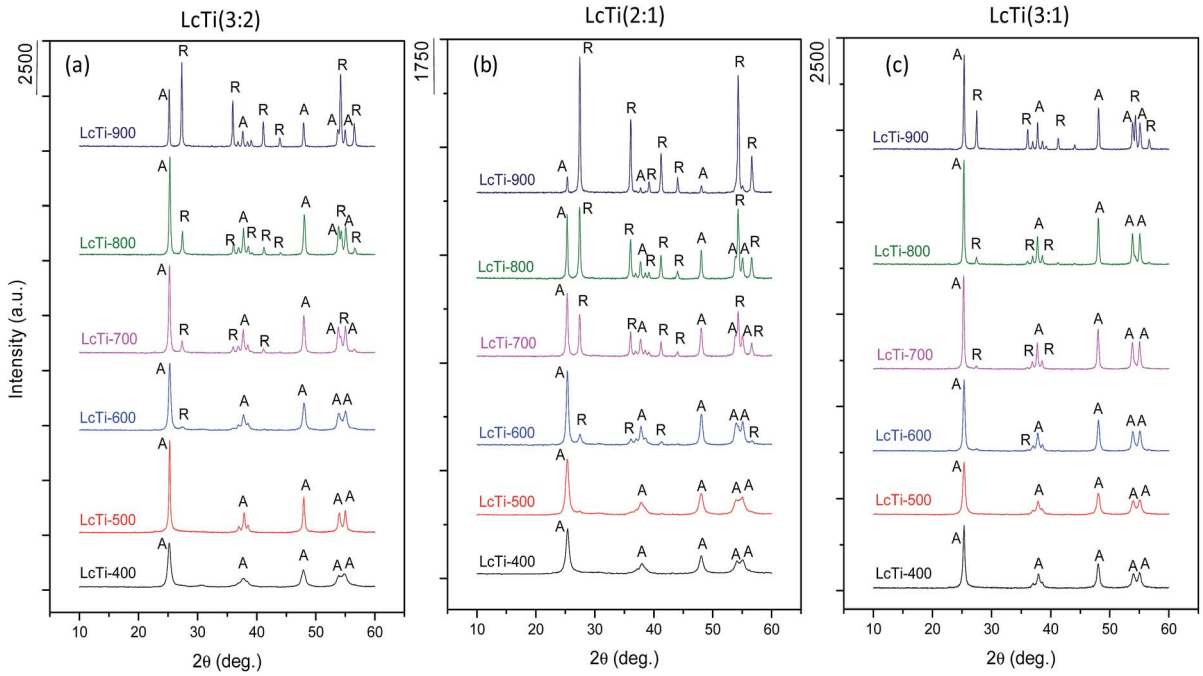

Fig. 5 XRD patterns of the micron-sized buckyball-like TiO_2 architectures synthesized *via* different precursor loadings: (a) LcTi(3 : 2); (b) LcTi(2 : 1) and (c) LcTi(3 : 1) which were calcined in air at 400, 500, 600, 700, 800, and 900 °C for 3 h after the synthesis. "A" and "R" stand for anatase and rutile phases; respectively.

XRD data (Fig. 5). It is well-known that anatase phase has six ($1A_{1g}$, $2B_{1g}$ and $3E_g$) and the rutile phase has five (B_{1g}, multi-proton process, E_g, A_{1g} and B_{2g}) characteristic Raman active modes.[31] Due to spectral overlap, poorly ordered phases with relatively smaller crystallite sizes, and contributions from phonon bands originating from the polymer network of the residual LC biotemplate (*i.e.*, features marked with ♣ symbol in Fig. 7), only four prominent anatase peaks at 142 cm^{-1} (E_g), 393 cm^{-1} (B_{1g}), 514 cm^{-1} (A_{1g}), and 638 cm^{-1} (E_g) and two rutile peaks at 446 cm^{-1} (E_g) and 609 cm^{-1} (A_{1g}) were discernible (Fig. 7). Consistent with the XRD results shown in Fig. 5, Raman data also suggested that lower calcination temperatures favored anatase phase, while the rutile content increased with increasing calcination temperatures.

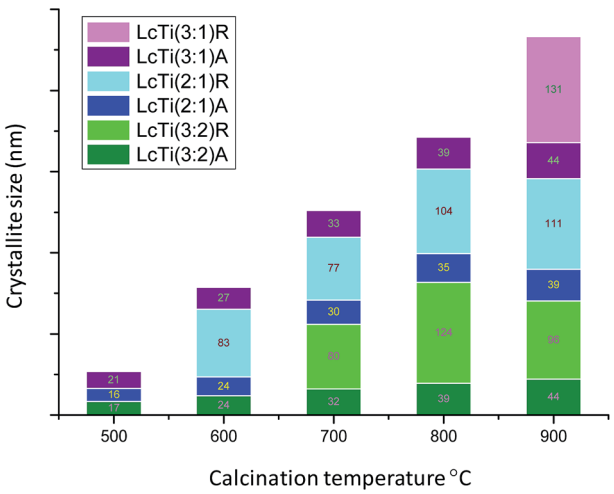

Fig. 6 Average crystallite sizes of various crystalline domains in the micron-sized buckyball-like TiO_2 architectures as a function of calcination temperature and precursor loading (estimated by the Scherrer equation; $d = k\lambda/\beta \cos(\theta_B)$; where d is the average crystallite diameter in nm; k is the shape factor, *i.e.*, 0.9; λ is the wavelength of the X-ray radiation source in nm; β is the full width at half maximum intensity in radians and θ_B is the Bragg angle).

Table 1 Relative weight percent values for anatase and rutile phases in the micron-sized buckyball-like TiO_2 architectures determined by Spurr and Myers approach[30]

Sample	Weight percent of anatase (%)	Weight percent of rutile (%)
LcTi(3 : 2)-400	100.0	0.0
LcTi(3 : 2)-500	100.0	0.0
LcTi(3 : 2)-600	95.4	4.6
LcTi(3 : 2)-700	85.9	14.1
LcTi(3 : 2)-800	77.0	23.0
LcTi(3 : 2)-900	35.0	65.0
LcTi(2 : 1)-400	100.0	0.0
LcTi(2 : 1)-500	100.0	0.0
LcTi(2 : 1)-600	85.6	14.4
LcTi(2 : 1)-700	**54.5**	**45.5**
LcTi(2 : 1)-800	**41.7**	**58.3**
LcTi(2 : 1)-900	8.4	91.6
LcTi(3 : 1)-400	100.0	0.0
LcTi(3 : 1)-500	100.0	0.0
LcTi(3 : 1)-600	96.6	3.4
LcTi(3 : 1)-700	96.1	3.9
LcTi(3 : 1)-800	91.7	8.3
LcTi(3 : 1)-900	65.8	34.2

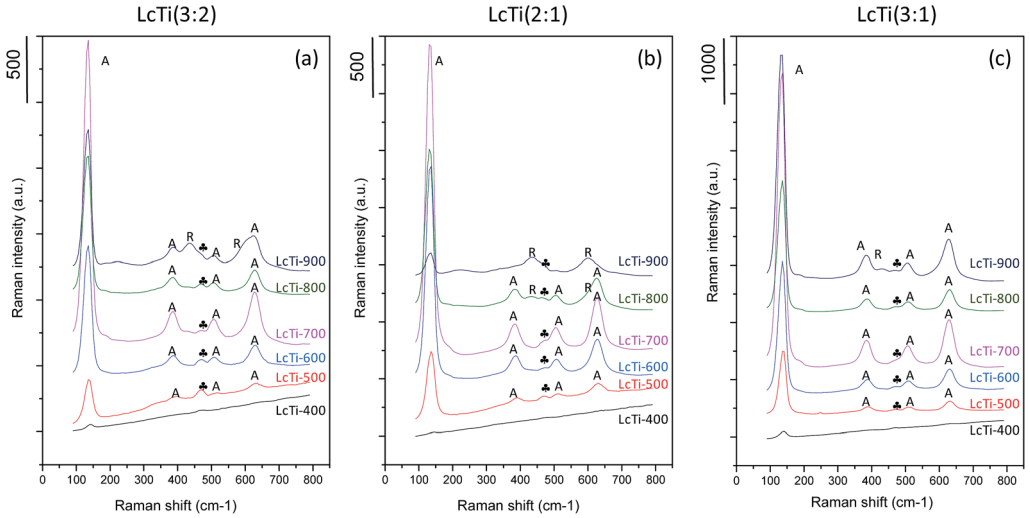

Fig. 7 Raman spectra of the micron-sized buckyball-like TiO_2 architectures synthesized *via* different precursor solutions: (a) LcTi(3 : 2); (b) LcTi(2 : 1) and (c) LcTi(3 : 1) which were calcined in air at 400, 500, 600, 700, 800 and 900 °C for 3 h after the synthesis; (A) TiO_2 anatase, (R) TiO_2 rutile, (♣) biopolymer.

Photocatalytic performance

Time-dependent photocatalytic RhB degradation performance of micron-sized buckyball-like TiO_2 architectures were examined under UVA irradiation and the apparent first-order rate constants (k') for RhB photodegradation were calculated as a function of calcination temperature and TIP loading in the precursor solution (Fig. 8). Note that the photocatalytic

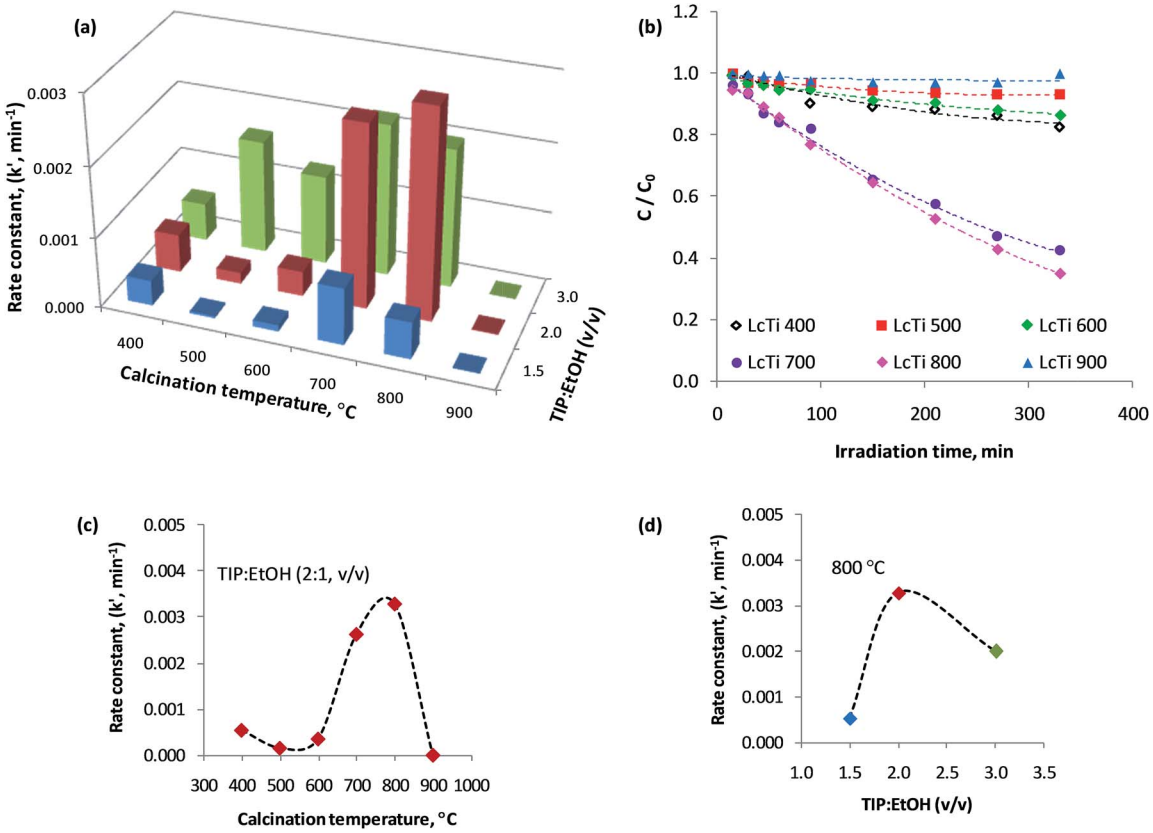

Fig. 8 The influence of the calcination temperature and the TIP : EtOH volume ratio on the apparent first-order rate constant (k') for the photocatalytic RhB degradation *via* micron-sized buckyball-like TiO_2 architectures under UVA illumination at room temperature; (a) k' values as a function of composition and calcination temperature, (b) corresponding plots for C/C_0 *vs.* time curves, (c) variation of k' as a function of calcination temperature for LcTi(2 : 1), (d) variation of k' as a function of TIP : EtOH (v/v) ratio for the samples calcined at 800 °C.

oxidation experiments could not be realized for those samples calcined at lower temperatures (<400 °C) due to low density of the corresponding solid photocatalysts and presence of their high biomaterial content (which lead to the floating of the photocatalyst powders on the aqueous medium, preventing efficient mixing and homogenous UVA exposure).

Fig. 8a and b illustrates the relative decolorization performances of the photocatalysts. Before the UVA illumination, RhB dye was kept in contact with the photocatalyst under dark conditions for 1 h. It was observed that after the adsorption–desorption equilibrium was reached (under dark conditions), only a small amount of RhB dye (~0.9–2.0% of the initial RhB concentration) was adsorbed on the photocatalyst surface. Thus, photodegradation results were corrected using this "dark" control experiment. As a second control experiment, we also checked the self-degradation of RhB under UV illumination in the absence of any photocatalysts. Hence, RhB self-degradation was also taken into account for reporting the final photodegradation results.

From the data presented in Fig. 8a it can be concluded that among all of the investigated micron-sized buckyball-like TiO_2 architectures, LcTi(2 : 1)-800 sample has the highest k' value. Fig. 8c illustrates that the photocatalytic performance of the LcTi(2 : 1) sample increases with increasing calcination temperature and reaches its highest value at 800 °C. After this optimum temperature, photocatalytic activity falls in a drastic manner. Presented data from XRD and Raman spectroscopy in Fig. 5–7, suggest that there is an optimum anatase/rutile weight ratio (*viz.*, 1 : 1) that leads to an optimum photocatalytic performance. This optimum phase composition is reached at a calcination temperature of 800 °C; at higher temperatures than 800 °C, TiO_2 domains become enriched in rutile and lose their activities.

Fig. 8d demonstrates the effect of TIP precursor loading for the photocatalysts calcined at the optimum calcination temperature of 800 °C. It is shown that for low TIP/EtOH ratios (*i.e.*, LcTi(3 : 2)-800), there is simply not enough active sites. For the intermediate TIP/EtOH value, the photocatalytic activity is maximized and for higher TIP/EtOH ratios, photocatalytic activity starts to decline. Drop in the photocatalytic activity at higher TIP loadings can presumably be attributed to sintering of the TiO_2 domains and deviations in the relative anatase : rutile compositional ratio from the optimal value.

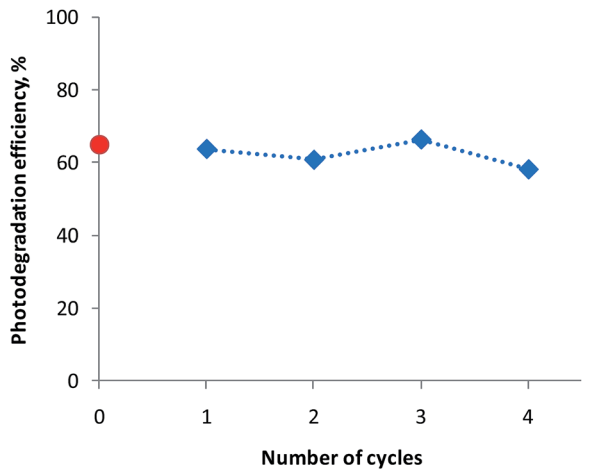

Fig. 9 Reusability of the LcTi(2 : 1)-800 catalyst under UVA illumination at room temperature.

Repeatability of the photocatalytic performance

The reusability of the photocatalyst is important for the practical applications relevant to the photodegradation of organic contaminants in water. Among all of the investigated micron-sized buckyball-like TiO_2 architectures, LcTi(2 : 1)-800 sample which has the highest k' value was selected to demonstrate the reusability performance. For this purpose, using the identical experimental conditions described above, photocatalytic performance studies were repeated for multiple successive catalytic runs. In these experiments, an initial 25 mg of LcTi(2 : 1)-800 sample was used which was re-collected from the suspension after each run and directly used in the next catalytic run.

Fig. 9 represents the % photodegradation efficiency values (*i.e.* $((C_0 - C)/C_0) \times 100$) obtained after 330 min of irradiation for each run. The red data point in Fig. 9 corresponds to the performance of the fresh catalyst whose behaviour was presented earlier (Fig. 8b) while the blue data points represent the successive runs where the fresh catalyst was re-used multiple times. As can be seen from Fig. 9, catalytic performance of the catalyst is conserved to a great extent after multiple runs without a significant indication of catalytic deactivation.

Conclusions

In the current work, we presented a simple sol–gel synthesis method for the production of micron-sized buckyball-like TiO_2 architectures using *Lycopodium clavatum* (LC) spores as biotemplates. We demonstrated that by simply altering the titanium(IV) isopropoxide : ethanol volume ratio in the synthesis mixture, as well as the calcination temperature, one could fine-tune the crystal structure and the surface composition of the buckyball-like TiO_2 overlayer. It was also illustrated that the unique surface morphologies and pore structures of the LC biotemplates could be successfully transferred to the inorganic TiO_2 overlayer, followed by an effective removal of the biological scaffold. Moreover, we demonstrated the photocatalytic functionality and catalytic reusability of micron-sized buckyball-like TiO_2 architectures in the photocatalytic degradation of Rhodamine B dye. It was shown that the photocatalytic activity of the TiO_2 overlayer could be modified in a controlled manner by adjusting the relative surface coverage of anatase and rutile domains. These results open a potential gateway for the synthesis of a large variety of bio-inspired material families comprised of reducible metal oxides (*e.g.*, TiO_2, CeO_2, ZrO_2, ZnO, Fe_2O_3, Fe_3O_4 *etc.*), metal sulfides (*e.g.*, CdS, PbS *etc.*), mixed-metal oxides (*e.g.*, TiO_2–Al_2O_3, TiO_2–ZrO_2, CeO_2–ZrO_2, TiO_2–ZnO, *etc.*) and/or perovskites (*e.g.*, $LaCoO_3$, $LaMnO_3$ *etc.*) with unprecedented surface/electronic/photonic properties. Moreover, functionalization of such novel bio-inspired metal oxide systems with transition metal nanoparticles such as Au,

Cu, Pd, Pt, Ag and/or ionic liquids could yield new material platforms and provide invaluable opportunities in catalysis, plasmonics, sensor technologies, energy applications, pharmaceutics, medicine, and nanotechnology. Further studies are underway in our research group to elucidate the high thermal catalytic performance of micron-sized buckyball-like TiO_2 architectures decorated with mono-dispersed Ru nanoparticles in formic acid dehydrogenation as well as NH_3BH_3 dehydrogenation.

Acknowledgements

The authors acknowledge the financial support from the Scientific and Technological Research Council of Turkey (TUBITAK) (Project Code: 113Z543) and the USA National Science Foundation (NSF EAGER Award 1346596).

Notes and references

1 K. J. K. Van Bommel, A. Friggeri and S. Shinkai, *Angew. Chem., Int. Ed.*, 2003, **42**, 980–999.
2 C. Sanchez, H. Arribart and M. M. G. Guille, *Nat. Mater.*, 2005, **4**, 277–288.
3 S. Sotiropoulou, Y. Sierra-sastre, S. S. Mark and C. A. Batt, *Chem. Mater.*, 2008, **20**, 821–834.
4 M. R. Jones, K. D. Osberg, R. J. Macfarlane, M. R. Langille and C. A. Mirkin, *Chem. Rev.*, 2011, **111**, 3736–3827.
5 O. Paris, I. Burgert and P. Fratzl, *MRS Bull.*, 2010, **35**, 219–226.
6 H. Zhou, T. Fan and D. Zhang, *ChemSusChem*, 2011, **4**, 1344–1387.
7 X. Wang, Z. Li, J. Shi, Y. Yu, *Chem. Rev.*, 2014, **114**, 9346–9384.
8 X. Chen and S. S. Mao, *Chem. Rev.*, 2007, **107**, 2891–2959.
9 M. A. Henderson, *Surf. Sci. Rep.*, 2011, **66**, 185–297.
10 M. Dahl, Y. Liu and Y. Yin, *Chem. Rev.*, 2014, **114**, 9853–9889.
11 K. Liu, M. Cao, A. Fujishima and L. Jiang, *Chem. Rev.*, 2014, **114**, 10044–10094.
12 F. C. Meldrum and H. Cölfen, *Chem. Rev.*, 2008, **108**, 4332–4432.
13 A. Chen, J. Qian, Y. Chen, X. Lu, F. Wang and Z. Tang, *Powder Technol.*, 2013, **249**, 71–76.
14 Z. He, W. Que and Y. He, *Mater. Lett.*, 2013, **94**, 136–139.
15 K.-J. Hwang, D. Kang, S. Lee, C.-H. Hwang, C. Kim, N. Kim, S. Jin, I.-H. Lee and J.-Y. Park, *Mater. Lett.*, 2014, **115**, 265–267.
16 J. Brooks and G. Shaw, *Grana*, 1978, **17**, 91–97.
17 W. Li, Z. Wu, J. Wang, A. A. Elzatahry and D. Zhao, *Chem. Mater.*, 2014, **26**, 287–298.
18 L. Liu and X. Chen, *Chem. Rev.*, 2014, **114**, 9890–9918.
19 N. Ballard and S. A. F. Bon, *Polym. Chem.*, 2011, **2**, 823–827.
20 S. Barrier, A. Diego-Taboada, M. J. Thomasson, L. Madden, J. C. Pointon, J. D. Wadhawan, S. T. Beckett, S. L. Atkin and G. Mackenzie, *J. Mater. Chem.*, 2011, **21**, 975–981.
21 H. M. Daluz, *Fundamentals of Fingerprint Analysis*, Taylor and Francic Group, USA, 2014.
22 M. Niederberger and H. Cölfen, *Phys. Chem. Chem. Phys.*, 2006, **8**, 3271–3287.
23 X. Li, G. Sun, Y. Li, J. C. Yu, J. Wu, G.-H. Ma and T. Ngai, *Langmuir*, 2014, **30**, 2676–2683.
24 Y.-P. Zhu, T.-Y. Ma, T.-Z. Ren, J. Li, G.-H. Du and Z.-Y. Yuan, *Appl. Catal., B*, 2014, **156–157**, 44–52.
25 M. Xiong, L. Chen, Q. Yuan, J. He, S. Luo and S. Yin, *Dalton Trans.*, 2014, 8331–8337.
26 D. A. Erdogan, M. Polat, R. Garifullin, M. O. Guler and E. Ozensoy, *Appl. Surf. Sci.*, 2014, **308**, 50–57.
27 M. El-Roz, Z. Haidar, L. Lakiss, J. Toufaily and F. Thibault-Starzyk, *RSC Adv.*, 2013, **3**, 3438–3445.
28 M. Benítez-Guerrero, L. A. Pérez-Maqueda, P. E. Sánchez-Jiménez and J. Pascual-Cosp, *Microporous Mesoporous Mater.*, 2014, **185**, 167–178.
29 N. Kocak, M. Sahin and I. H. Gubbuk, *J. Inorg. Organomet. Polym. Mater.*, 2012, **22**, 852–859.
30 R. A. Spurr and H. Myers, *Anal. Chem.*, 1957, **29**, 760–762.
31 T. Ohsaka, F. Izumi and Y. Fujiki, *J. Raman Spectrosc.*, 1978, **7**, 321–324.

